Inorganic Chemistry

pubs.acs.org/IC Article

Expansion of the Family of Molecular Nanoparticles of Cerium Dioxide and Their Catalytic Scavenging of Hydroxyl Radicals

Kylie J. Mitchell, Justin L. Goodsell, Bradley Russell-Webster, Umar T. Twahir, Alexander Angerhofer, Khalil A. Abboud, and George Christou*

Cite This: *Inorg. Chem.* 2021, 60, 1641−1653

Read Online

ACCESS | Metrics & More | Article Recommendations | SI Supporting Information

ABSTRACT: The syntheses, crystal structures, and catalytic radical scavenging activity are reported for four new molecular clusters that have resulted from a bottom-up molecular approach to nanoscale CeO_2. They are $[Ce_6O_4(OH)_4(dmb)_{12}(H_2O)_4]$ (dmb^- = 2,6-dimethoxybenzoate), $[Ce_{16}O_{17}(OH)_6(O_2CPh)_{24}(HO_2CPh)_4]$, $[Ce_{19}O_{18}(OH)_9(O_2CPh)_{27}(H_2O)(py)_3]$, and $[Ce_{24}O_{27}(OH)_9(O_2CPh)_{30}(py)_4]$. They represent a major expansion of our family of so-called "molecular nanoparticles" of this metal oxide to seven members, and their crystal structures confirm that their cores all possess the fluorite structure of bulk CeO_2. In addition, they have allowed the identification of surface features such as the close location of multiple Ce^{3+} ions and organic ligand binding modes not seen previously. The ability of all seven members to catalytically scavenge reactive oxygen species has been investigated using $HO^•$ radicals, an important test reaction in the ceria nanoparticle biomedical literature, and most have been found to exhibit excellent antioxidant activities compared to traditional ceria nanoparticles, with their activity correlating inversely with their surface Ce^{3+} content.

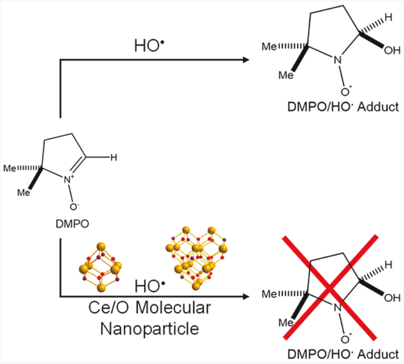

INTRODUCTION

Cerium dioxide nanoparticles (CNPs, nanoceria) are widely used in catalysis, mechanical polishing, solid-oxide fuel cells, UV shielding, and other applications.[1−7] CNPs are useful and reactive materials because of the general advantage of nanoparticles in that they possess a high surface area to volume ratio but also because of the increased amount of Ce^{3+} present on the surface relative to the bulk material and the ease with which Ce can switch between the trivalent and tetravalent oxidation state. Bulk CeO_2 possesses a fluorite structure (Figure 1) comprising alternating layers of Ce^{4+} ions with an 8-coordinate cubic geometry and O^{2-} ions with tetrahedral geometry. This fluorite lattice allows for the creation of oxygen vacancies with the concomitant reduction of Ce^{4+} to Ce^{3+}, contributing to the overall reactivity of these nanoparticles.[8−13]

CNPs have recently gained increasing attention because of their higher reactivity at lower temperatures and even room temperature, especially in the area of nanomedicine.[7,14−20] This is largely due to the catalytic scavenging (antioxidant) ability of CNPs to various reactive oxygen species (ROS): with superoxide (O_2^-) radicals and hydrogen peroxide (H_2O_2), they can show superoxide dismutase and catalase mimetic behavior, respectively, depending on different variables such as the Ce^{3+}/Ce^{4+} ratio, size, morphology, surface coatings, and environmental conditions.[21−25] They have also demonstrated catalytic scavenging of extremely dangerous hydroxyl ($HO^•$) radicals.[26] Xue et al. demonstrated that 5−10 nm CNPs have a greater antioxidant activity than 15−20 nm CNPs because of the

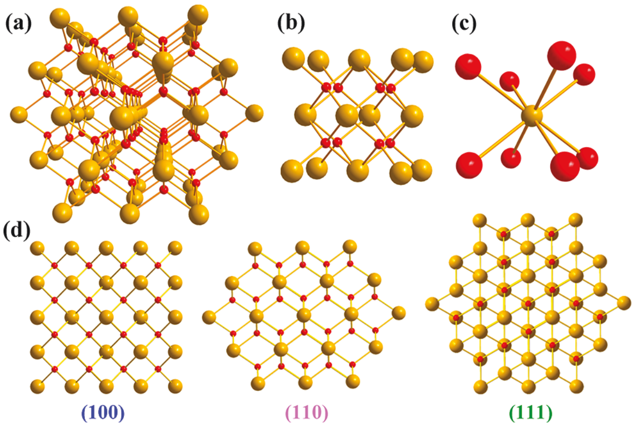

Figure 1. (a) Fluorite structure of CeO_2 emphasizing the alternating layers of Ce^{4+} and O^{2-} ions. (b) Unit cell of the CeO_2 structure. (c) Single Ce^{4+} ion showing its 8-coordination to oxide ions and its cubic geometry. (d) Three low-index faces of CeO_2 color coded as the corresponding facets in the structural figures below. Color code: Ce^{4+}, gold; O, red.

Received: October 22, 2020
Published: January 12, 2021

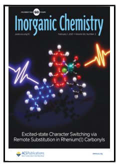

ACS Publications

https://dx.doi.org/10.1021/acs.inorgchem.0c03133

increased surface density of Ce^{3+} for the smaller nanoparticles, therefore enabling them to scavenge a greater amount of $HO^•$.[27] However, the prooxidant (radical-generating) ability of CNPs has also been reported through a possible Fenton-like reaction.[28] Similarly, Lu et al. demonstrated that several factors, such as the $OH^−$ concentration and the size, morphology, and concentration of CNPs, could result in conversion between the antioxidant and oxidant activity.[28] In addition, other factors such as the synthetic methods, composition, surface charge, and particle aggregation have been suggested as possible causes for CNP toxicity.[29,30]

Owing to the immense promise of CNPs to serve as antioxidants, there is a need for additional well-controlled studies to address which factors affect their reactivity in a beneficial way and which ones result in toxic conditions. However, this is extremely challenging given the usual problems with nanoparticles that samples consist of a range of size, shape, and surface features that cannot be easily controlled; for CNPs, even the Ce^{3+}/Ce^{4+} ratio is difficult to determine with confidence. Thus, a different approach is needed to overcome such limitations and allow the factors that control the reactivity to be addressed in a controlled manner.

We recently demonstrated an alternative, bottom-up molecular approach to ultrasmall (<3 nm) nanoparticles of CeO_2, synthesizing them instead as molecular clusters using ambient-temperature solution methods with simple carboxylate and pyridine ligands. This takes advantage of the benefits provided by molecular chemistry, such as products that are truly identical in size and shape and whose solubility and crystallinity allow structural characterization to atomic precision by single-crystal X-ray crystallography;[31,32] we now call such species "molecular nanoparticles". The initial breakthrough was the synthesis and characterization of Ce_{24} (**1**), Ce_{38} (**2**), and Ce_{40} (**3**) members, which have core diameters of 1−2 nm and display the fluorite structure of bulk CeO_2, a sine qua non for a true molecular nanoparticle of a metal oxide. They are thus true molecular pieces of CeO_2, i.e., ultrasmall nanoparticles. Prior to the isolation of **1**−**3**, there were very few known Ce/O clusters, most of them being nuclearity Ce_6,[40,41] the smallest unit of the CeO_2 fluorite lattice, and the largest being Ce_{22}.[42] Very recently, Farha and co-workers reported two clusters with Ce/O cores identical with those of **2** but with differing carboxylate ligands.[43]

Here we report significant enlargement of the family of Ce/O molecular nanoparticles in both the size and Ce^{3+}/Ce^{4+} ratio through the synthesis and structural characterization to atomic precision of four new members: $[Ce_6O_4(OH)_4(H_2O)_4(dmb)_{12}]$ (Ce_6; **4**; $dmb^−$ = anion of dimethoxybenzoic acid), $[Ce_{16}O_{17}(OH)_6(O_2CPh)_{24}(HO_2CPh)_3(H_2O)]$ (Ce_{16}; **5**), $[Ce_{19}O_{18}(OH)_9(O_2CPh)_{27}(H_2O)(py)_3]$ (Ce_{19}; **6**), and $[Ce_{24}O_{27}(OH)_9(O_2CPh)_{30}(py)_4]$ (Ce_{24}; **7**), which is similar to the previously reported Ce_{24} (**1**) but possesses an additional Ce^{3+} ion. With a family of seven atomically precise Ce/O molecular nanoparticles now available, we have been able to expand our knowledge of the types of surface features that can exist on these ultrasmall nanoparticles of CeO_2 and have also investigated their catalytic ROS scavenging ability as a function of the size and Ce^{3+}/Ce^{4+} ratio through the use of spin-trap techniques in conjunction with electron paramagnetic resonance (EPR) spectroscopy. We herein describe these results.

■ EXPERIMENTAL SECTION

Syntheses. All manipulations were performed under aerobic conditions using chemicals and solvents as received, unless otherwise stated. $[Ce_{24}O_{28}(OH)_8(PhCO_2)_{30}(py)_4]$ (**1**), $[Ce_{38}O_{54}(OH)_8(EtCO_2)_{36}(py)_8]$ (**2**), and $[Ce_{40}O_{54}(OH)_4(MeCO_2)_{46}(py)_4]$ (**3**) were prepared as reported previously.[31]

$[Ce_6O_4(OH)_4(H_2O)_4(dmb)_{12}]$ (4). To a stirred solution of 2,6-dimethoxybenzoic acid (dmbH; 1.5 g, 8.0 mmol) in $MeNO_2$ (15 mL) was added $Fe(NO_3)_3{\cdot}9H_2O$ (0.40 g, 1.0 mmol), $(NH_4)_2[Ce(NO_3)_6]$ (0.55 g, 1.0 mmol), and NEt_3 (1.1 mL, 8.0 mmol), which caused the solution to turn dark red and begin to deposit a white precipitate. The slurry was stirred a further 10 min and filtered, and the filtrate was allowed to stand undisturbed for 2 days at room temperature, during which time large yellow block-shaped crystals of **4**·$8MeNO_2{\cdot}2H_2O$ slowly formed. The crystals were collected by filtration, washed with $MeNO_2$, and dried in a vacuum. The yield was 79% based on Ce. The solid is hygroscopic. Anal. Calcd (found) for **4**·$3MeNO_2{\cdot}5H_2O$ ($C_{111}H_{139}N_3Ce_6O_{47}$): C, 38.05 (37.69); H, 4.00 (3.50); N, 1.20 (1.28). Selected IR data (KBr disk, cm^{-1}): 3457 (mb), 2941 (w), 2838 (w), 1595 (s), 1557 (s), 1473 (s), 1403 (s), 1251 (s), 1174 (w), 1142 (w), 1109 (s), 1029 (w), 838 (w), 816 (w), 769 (w), 736 (w), 631 (w), 596 (w), 551 (m).

$[Ce_{16}O_{17}(OH)_6(O_2CPh)_{24}(HO_2CPh)_4]$ (5). To a stirred solution of $PhCO_2H$ (0.98 g, 8.0 mmol) in acetonitrile (MeCN; 15 mL) was added $Fe(NO_3)_3{\cdot}9H_2O$ (0.40 g, 1.0 mmol), $(NH_4)_2[Ce(NO_3)_6]$ (0.55 g, 1.0 mmol), and NEt_3 (1.1 mL, 8.0 mmol), which caused the solution to turn dark red and begin to deposit a white precipitate. The slurry was stirred a further 10 min and filtered, and the filtrate was allowed to stand undisturbed for 2 weeks at room temperature, during which time yellow block-shaped crystals of **5**·$15MeCN{\cdot}5H_2O$ slowly formed. The crystals were collected by filtration, washed with MeCN, and dried in a vacuum. The yield was 7% based on Ce. Anal. Calcd (found) for **5**·2MeCN ($C_{193}H_{152}N_2Ce_{16}O_{78}$): C, 39.25 (39.34); H, 2.59 (2.77); N, 0.47 (0.50). Selected IR data (KBr disk, cm^{-1}): 3435 (mb), 3061 (w), 1594 (m), 1534 (s), 1492 (w), 1448 (w), 1403 (s), 1307 (w), 1178 (w), 11070 (w), 1025 (w), 849 (w), 716 (s), 687 (w), 584 (w), 510 (m), 427 (m).

$[Ce_{19}O_{18}(OH)_9(O_2CPh)_{27}(H_2O)(py)_3]$ (6). To a stirred solution of pyridine/water (H_2O; 10:1 mL, v/v) was added $(NH_4)_2[Ce(NO_3)_6]$ (0.55 g, 1.0 mmol), $PhCO_2H$ (0.24 g, 2.0 mmol), and NH_4I (0.14 g, 1.0 mmol). The golden-yellow solution was stirred for 30 min, followed by the addition of 20 mL of MeCN. The solution was then maintained undisturbed for 3 days at room temperature, during which time X-ray-quality yellow square plates of **6**·3.5py·8MeCN formed. The crystals were collected by filtration, washed with MeCN, and dried in a vacuum. The yield was 25% based on Ce. The dried solid was hygroscopic. Anal. Calcd (found) for **6**·$12H_2O{\cdot}{}^1/_2MeCN$ ($C_{205}H_{185.5}N_{3.5}Ce_{19}O_{94}$): C, 35.87 (35.18); H, 2.64 (2.67); N, 0.71 (1.00). Selected IR data (KBr disk, cm^{-1}): 3430 (mb), 3134 (mb), 1594 (m), 1534 (s), 1492 (w), 1447 (w), 1402 (s), 1307 (w), 1178 (w), 1069 (w), 1025 (w), 849 (w), 717 (s), 688 (w), 558 (w), 514 (m), 489 (m), 406 (s).

$[Ce_{24}O_{27}(OH)_9(O_2CPh)_{30}(py)_4]$ (7). To a stirred solution of pyridine (10 mL) were added $Ce(NO_3)_3{\cdot}6H_2O$ (0.43 g, 1.0 mmol) and $PhCO_2H$ (0.24 g, 2.0 mmol). The colorless solution was stirred for 30 min, followed by the addition of 20 mL of MeCN. The solution was then maintained undisturbed for 1 week at room temperature, during which time X-ray-quality brown square plates of **7**·3.75py formed. The crystals were collected by filtration, washed with MeCN, and dried in a vacuum. The yield was 30% based on Ce. Anal. Calcd (found) for **7**·3py ($C_{245}H_{193}N_7Ce_{24}O_{96}$): C, 36.18 (36.37); H, 2.39 (2.41); N, 1.21 (1.22). Selected IR data (KBr disk, cm^{-1}): 3433 (w), 3064 (m), 1594 (s), 1537 (s), 1492 (w), 1448 (w), 1405 (s), 1307 (w), 1178 (w), 1142 (w), 1070 (w), 1025 (w), 849 (w), 717 (s), 679 (w), 558 (w), 513 (m), 488 (m), 408 (s).

5,5-Dimethyl-1-pyrroline *N*-Oxide (DMPO) Spin-Trap Sample Preparation. Immediately before the EPR measurements, each sample was prepared by mixing aqueous solutions of H_2O_2 (20 μL, 10

Table 1. Crystal Data and Structure Refinement Parameters for 4−7

	4·8MeNO$_2$·2H$_2$O	**5**·15MeCN·5H$_2$O	**6**·3.5py·8MeCN	**7**·7.5py
formula[a]	$C_{116}H_{144}Ce_6N_8O_{78}$	$C_{226}H_{182}Ce_{16}N_{15}O_{78}$	$C_{235}H_{199}Ce_{19}N_{14}O_{81}$	$C_{267.5}H_{215.5}Ce_{24}N_{11.5}O_{96}$
fw, g mol^{-1}	3739.10	6498.69	7185.35	8489.88
space group	$P\bar{1}$	$Pa\bar{3}$	$P2_1/n$	$P2_1/n$
a, Å	14.8430(9)	35.4805(7)	19.7865(11)	21.8374(17)
b, Å	16.1982(10)	35.4805(7)	35.949(2)	26.302(2)
c, Å	17.5748(11)	35.4805(7)	35.343(2)	24.988(2)
α, deg	64.7932(10)	90	90	90
β, deg	70.8862(11)	90	92.1055(12)	90.845(2)
γ, deg	71.3192(11)	90	90	90
V, Å^3	3530.6(4)	44665(3)	25123(3)	14351(2)
Z	1	8	4	2
T, K	100(2)	100(2)	100(2)	100(2)
λ,[b] Å	0.71073	0.71073	0.71073	0.71073
ρ_{calc}, g cm^{-3}	1.759	1.933	1.900	1.939
μ, mm^{-1}	2.003	3.279	3.449	3.804
R_1[c,d]	0.0277	0.0662	0.0793	0.0938
wR_2[e]	0.0684	0.1768	0.1885	0.2338

[a] Including solvent molecules. [b] Graphite monochromator. [c] $I > 2\sigma(I)$. [d] $R_1 = 100\sum(||F_o| - |F_c||)/\sum|F_o|$. [e] $wR_2 = 100[\sum[w(F_o^2 - F_c^2)^2]/\sum[w(F_o^2)^2]]^{1/2}$, with $w = 1/[\sum^2(F_o^2) + [(ap)^2 + bp]$, where $p = [\max(F_o^2,0) + 2F_c^2]/3$.

mM), DMPO (32 μL, 0.5 mM), and the ceria molecular nanoparticle (40 μL, 1 mM). FeCl$_2$ (20 μL, 10 mM) was added last to generate OH$^\bullet$ radicals. Upon the addition of FeCl$_2$, a timer was started to ensure that each sample had the same time to react. The mixture was vortexed for 10 s and immediately transferred to a capillary. After 1 min of total time, the first EPR spectrum of the time scan was recorded. Successive scans were recorded at 1 min intervals for a total time course of 10 min. For the control samples, the same procedure as that above was followed, except that the addition of ceria molecular nanoparticles was replaced with an equal volume of H$_2$O. Additional control experiments with each nanocluster were carried out by replacing FeCl$_2$ with an equal volume of H$_2$O.

X-ray Crystallography. Data were collected at 100 K on a Bruker DUO diffractometer using Mo Kα radiation (λ = 0.71073 Å) and an APEXII CCD area detector. Raw data frames were read by the program *SAINT*[33] and integrated using 3D profiling algorithms. The resulting data were reduced to produce *hkl* reflections and their intensities and estimated standard deviations. The data were corrected for Lorentz and polarization effects, and numerical absorption corrections were applied based on indexed and measured faces. The structures were solved and refined in *SHELXTL2013*[34] for **4**·8MeNO$_2$·2H$_2$O and *SHELXTL2014*[35] for the others using full-matrix least-squares cycles. Refinements were carried out by minimizing the wR_2 function using F^2 rather than F values. R_1 is calculated to provide a reference to the conventional R value, but its function is not minimized. Non-H atoms were refined with anisotropic thermal parameters, and all H atoms were calculated in idealized positions and refined riding on their parent atoms. All crystal data and refinement details are collected in Table 1.

For **4**·8MeNO$_2$·2H$_2$O, the asymmetric unit consists of a half Ce$_6$ cluster on an inversion center, a H$_2$O molecule, and four MeNO$_2$ solvent molecules. The core O^{2-} (O1−O4) and OH$^-$ (O1′−O4′) ions were disordered but, owing to their different Ce−O bond lengths, could be resolved at each position, refining to ∼50:50% occupancies. The MeNO$_2$ molecules were too disordered to be modeled properly; thus, the program *SQUEEZE*,[36] a part of the *PLATON*[37] package of crystallographic software, was used to calculate the solvent disorder area and remove its contribution to the overall intensity data. The O atom of the trapped H$_2$O molecule, O31, was slightly disordered and was refined in two positions; the two H atoms were not disordered and were obtained from a difference Fourier map and refined freely. Similarly, the H atoms on the H$_2$O ligands, O29 and O30, were refined freely. In the final cycle of refinement, 16226 reflections [of which 14605 are observed with $I > 2\sigma(I)$] were used to refine 839 parameters, and the resulting R_1, wR_2, and S (goodness of fit) were 2.77%, 6.84%, and 1.085, respectively.

For **5**·15MeCN·5H$_2$O, the asymmetric unit consists of $^1/_3$ of a Ce$_{16}$ cluster on a 3-fold rotation axis and ∼5 MeCN and ∼1.7 H$_2$O solvent molecules. The MeCN molecules were too disordered to be modeled properly; thus, the program *SQUEEZE*[36] was again used to calculate the solvent disorder area and remove its contribution to the overall intensity data. Owing to the proximity of the H$_2$O molecules to the disordered parts of the cluster, the H$_2$O molecules could not be removed by *SQUEEZE*[36] and were refined in the final cycles at five positions, O1′−O5′, two with occupancies of 40% and three with 30%. One benzoate ligand (C51−C57) was disordered about two parts, with the minor part (30%) being C51′−C57′. The H atoms on O2, O5, and O9 were located from a difference Fourier map and refined freely with $^2/_3$ site occupancy factors consistent with the bond valence sum (BVS) values for O2, O5, and O9 that indicated partial-occupancy protonation. The H atom on O15 of the benzoic acid ligand was placed in an idealized position and refined riding on its parent atom. The H atom on the H$_2$O ligand, O7, could not be located and was thus not included in the final refinement model. In the final cycle of refinement, 13114 reflections [of which 6272 are observed with $I > 2\sigma(I)$] were used to refine 769 parameters, and the resulting R_1, wR_2, and S were 6.62%, 17.68%, and 0.914, respectively.

For **6**·3.5py·8MeCN, the asymmetric unit contains the complete Ce$_{19}$ cluster and 3.5 pyridine and 8 MeCN solvent molecules. All of the rings were constrained to maintain ideal geometry using the *AFIX 66* command. The MeCN molecules were too disordered to be modeled properly; thus, the program *SQUEEZE*[36] was again used to calculate the solvent disorder area and remove its contribution to the overall intensity data. One of the phenyl rings of a benzoate was disordered and was refined in two parts with 60:40% occupancies. An additional disorder occurred between a pyridine ligand and a H$_2$O ligand (50:50%) on Ce6. The pyridine solvent molecules were involved in N···H−O hydrogen bonding with surface μ_3-OH$^-$ ligands [N···O = 2.707(4)−2.940(4) Å]; one of them had 50% occupancy. In the final cycle of refinement, 44246 reflections [of which 17558 are observed with $I > 2\sigma(I)$] were used to refine 1400 parameters, and the resulting R_1, wR_2, and S were 7.93%, 18.85%, and 0.977, respectively.

For **7**·7.5py, the asymmetric unit consists of half of a Ce$_{24}$ cluster and 3.75 pyridine solvent molecules disordered over seven locations. One benzoate Ph ring was disordered about two positions. The H atoms on O atoms could not be located from difference Fourier maps; thus, four of them were placed in calculated idealized positions on O12, O14, O15, and O16, whose O BVS indicated that they were protonated. No H atoms were found on the N atoms of the lattice

Table 2. Formulas and Details of the Molecular Nanoparticles 1−7

formula[a]	oxidation state	$n(100)$[b]	ref[c]
$[Ce_{24}O_{28}(OH)_8(O_2CPh)_{30}(py)_4]$ (**1**)[d]	$22Ce^{4+}$, $2Ce^{3+}$	4	31
$[Ce_{38}O_{54}(OH)_8(O_2CEt)_{36}(py)_8]$ (**2**)	$38Ce^{4+}$	6	31
$[Ce_{40}O_{54}(OH)_4(O_2CMe)_{46}(py)_4]$ (**3**)	$38Ce^{4+}$, $2Ce^{3+}$	6	31
$[Ce_6O_4(OH)_4(dmb)_{12}(H_2O)_4]$ (**4**)	$6Ce^{4+}$	0	t.w.
$[Ce_{16}O_{17}(OH)_6(O_2CPh)_{24}(HO_2CPh)_4]$ (**5**)	$16Ce^{4+}$	0	t.w.
$[Ce_{19}O_{18}(OH)_9(O_2CPh)_{27}(H_2O)(py)_3]$ (**6**)	$15Ce^{4+}$, $4Ce^{3+}$	3	t.w.
$[Ce_{24}O_{27}(OH)_9(O_2CPh)_{30}(py)_4]$ (**7**)[d]	$21Ce^{4+}$, $3Ce^{3+}$	4	t.w.

[a]Ignoring any ligand disorder. [b]Number of surface (100) Ce_4 squares. [c]t.w. = this work. [d]**1** and **7** are also referred to as Ce_{24A} and Ce_{24B}, respectively.

pyridine rings. Four pyridine solvent molecules (N931 and N951) were found hydrogen bonding to μ_3-OH^- ligands and thus were not disordered, and the others were disordered and/or had partial occupancies to various extents. In the final cycle of refinement, 25279 reflections [of which 15097 are observed with $I > 2s(I)$] were used to refine 1433 parameters, and the resulting R_1, wR_2, and S were 9.38%, 23.38%, and 1.500, respectively.

Physical Measurements. IR spectra were recorded in the solid state (KBr pellets) on a Nicolet Nexus 670 FTIR spectrometer in the 400−4000 cm^{-1} range. Elemental analyses (C, H, and N) were performed by the in-house facilities of the Chemistry Department, University of Florida, for **4** and at Atlantic Microlab, Inc., for **5**−**7**. EPR measurements were recorded on a Bruker ELEXSYS-II E500 with a Bruker 4116DM resonator mounted on an Oxford Instruments CF900 helium cryostat for low-temperature experiments. For **7**, data were collected at 5 K in the 50−7050 G field range temperature with the following parameters: power 6.32×10^{-1} mW; frequency 9.422733 GHz; modulation frequency 100.00 kHz; modulation amplitude 10.00 G; conversion time 80.00 ms; 4000 data points. For **6**, data were collected at 10 K in the 50−7050 G field range with the following parameters: power 6.32×10^{-1} mW; frequency 9.649962 GHz; modulation frequency 100.00 kHz; modulation amplitude 10.00 G; conversion time 80.00 ms; 2048 data points. For the DMPO spin-trap experiments, data were collected using a Bruker SHQE resonator at room temperature in the 3435−3585 G field range with the following typical acquisition parameters: power 2.00 mW; frequency 9.86 GHz; modulation frequency 100.00 kHz; modulation amplitude 1.00 G; conversion time 40.00 ms; 1024 data points.

■ RESULTS AND DISCUSSION

Syntheses. Various reaction conditions were systematically explored before the procedures described were finalized. Although they may at first glance seem similar, they differ in several important ways. In addition to some variation in the carboxylate, there is (i) the presence or absence of Fe^{3+}, (ii) the presence or absence of a reducing agent (NH_4I), (iii) the presence or absence of py as a potential ligand, (iv) the reaction solvent being $MeNO_2$, MeCN, py/H_2O, and py/MeCN for **4**−**7**, respectively, and (v) the Ce reagent being $(NH_4)_2[Ce(NO_3)_6]$ or $Ce(NO_3)_3$. As a result, the reactions are perfectly reproducible as described, giving identical IR spectra for the product and the same unit cells when multiple crystals were examined.

Compounds **4** and **5** were obtained from the reaction of $Fe(NO_3)_3{\cdot}6H_2O$, $(NH_4)_2[Ce(NO_3)_6]$, NEt_3, and dbmH or $PhCO_2H$ in a 1:1:8:8 ratio in $MeNO_2$ or MeCN, respectively, leading to **4**·$8MeNO_2{\cdot}2H_2O$ and **5**·$15MeCN{\cdot}5H_2O$ in 79% and 7% yield, respectively. The Fe^{III} reagent arose from initial experiments targeting a Ce/Fe product and was retained because attempts to synthesize **4** and **5** in its absence were unsuccessful. The exact function of Fe is unclear, but we note that a previous Ce_6 complex could only be obtained in the presence of either Cu or Mn.[38] Other reagent ratios were systematically explored, but neither produced any isolable pure product or led to comparable or lesser yields.

Complexes **6** and **7** were synthesized in a manner similar to those reported by Mitchell et al.[31] Thus, $(NH_4)_2[Ce(NO_3)_6]$, $PhCO_2H$, and NH_4I in a 1:2:1 ratio in py/H_2O (10:1 mL) gave complex **6**·3.5py·8MeCN in 25% yield. **6** contains four Ce^{3+} ions and a different nuclearity than **1** (Ce_{24}), which was previously obtained in the absence of NH_4I, emphasizing the sensitivity of the obtained product nuclearity and Ce^{3+}/Ce^{4+} ratio to changes in the reaction conditions. Emphasizing further the latter point, the employment of a Ce^{3+} source, $Ce(NO_3)_3$, in place of $(NH_4)_2[Ce(NO_3)_6]$ in a $Ce(NO_3)_3$/$PhCO_2H$ reaction in a 1:2 ratio in py/MeCN (10:20 mL) gave instead **7**·3.75py in 30% yield. Complex **7** is structurally very similar to **1** but has an additional Ce^{3+} ion as determined by BVS calculations and EPR measurements (vide infra).

Description of Structures. For convenience, the full formulas and Ce oxidation states in **1**−**7** are collected in Table 2.

Complex **4** contains a $\{Ce_6(\mu_3\text{-}O)_4(\mu_3\text{-}OH)_4\}^{12+}$ core, comprising a $Ce^{4+}{}_6$ octahedron whose faces are bridged by μ_3-O^{2-} or μ_3-OH^- ions, a dmb^- bridging each Ce_2 edge in the common $\eta^1{:}\eta^1{:}\mu$ mode, and a terminal H_2O molecule on four Ce atoms (Figure 2). The Ce^{4+} oxidation states were confirmed by BVS calculations (Table S1).[39] Each face of the Ce octahedron is bridged by a μ_3-O atom that is either OH^- or O^{2-}. This is supported by the refinement, which shows each μ_3-O atom position refined as a 1:1 disordered mixture of μ_3-OH^- and O^{2-} (Table S2); the overall charge balance supports four O^{2-} and four OH^- being present. Ce2 and Ce3 are both 9-coordinate, while Ce1 is 8-coordinate. Other octahedral Ce^{4+} clusters have been reported previously but with slightly different $\{Ce_6(\mu\text{-}O)_x(\mu\text{-}OH)_{8-x}\}$ protonation levels and/or ligand types.[40−43]

Complex **5** (Figure 3) consists of a $\{Ce_{16}(\mu_4\text{-}O)_7(\mu_3\text{-}O)_{10}(\mu\text{-}OH)_6\}^{24+}$ core that clearly has the fluorite structure of bulk CeO_2, displaying alternating layers of cubic Ce^{4+} and tetrahedral O^{2-} ions. From the viewpoint of Figure 2, **5** has an A:B:B:A = 2:6:6:2 layered structure, but given its relatively low Ce_{16} nuclearity, all of its Ce ions are on the surface (Table S3). Thus, 4 Ce ions are 8-coordinate with distorted cubic geometry, and the other 12 ions are 9-coordinate; interestingly, all 16 of them are Ce^{4+}. The ligation is completed by 24 $PhCO_2^-$ and 4 monodentate $PhCO_2H$. A total of 12 of the $PhCO_2^-$ groups are in the common $\eta^1{:}\eta^1{:}\mu$-bridging mode, and the other 12 groups are $\eta^1{:}\eta^2{:}\mu$ chelating and bridging. Protons on the surface (i.e., μ_3-HO^-) were identified from O BVS (Table S4) and/or located crystallographically as being on O2, O5, and O9 and were given fixed occupancies of $^2/_3$

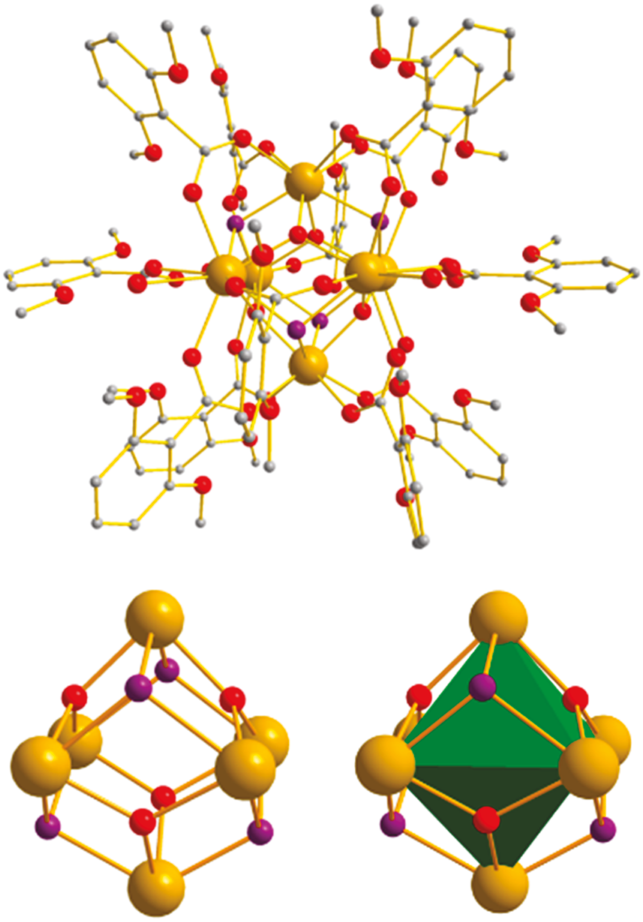

Figure 2. Full structure of complex **4** and its $\{Ce_6O_4(OH)_4\}^{12+}$ core. Color code: Ce^{4+}, gold; O, red; protonated O (i.e., OH^-), purple; C, gray; (111) facet, green. H atoms have been omitted for clarity.

consistent with the O BVS values, which with their symmetry-related partners gave a total of 6 surface μ_3-HO^- groups. The cluster has crystallographic C_3 and virtual T_d symmetry.

Complex **6** (Figure 4) consists of a $\{Ce_{19}O_{18}(OH)_9\}^{27+}$ core that again has the fluorite structure of CeO_2. There are four Ce^{3+} ions (Ce2, Ce17, Ce18, and Ce19), as confirmed by BVS calculations (Table S5), and as expected, they are all on the surface, three of them next to each other on one side of the molecule and the fourth on the other side. The Ce^{3+} ions do cause deviations of surface ions from ideal fluorite positions, but the overall fluorite structure is still retained. Five Ce^{4+} ions are 8-coordinate, and the others, including the Ce^{3+} ions, are 9-coordinate. There are 18 O^{2-} ions and 9 OH^- groups. The latter are all on the surface: 6 are μ_3-HO^- with trigonal-pyramidal O geometry and 3 are μ_3-HO^- with a T-shaped geometry unprecedented in our Ce/O clusters (vide infra). The H atoms were not observed, but their locations were identified from O BVS values (Table S6). The ligation is completed by 27 $PhCO_2^-$ and 3 py molecules, with 1 py disordered with the H_2O molecule coordinated to Ce6. The presence of unpaired electrons from Ce^{3+} ions was confirmed via EPR spectroscopy (Figure S1).

Complex **7** (Figure 5) is structurally nearly identical with the previously reported complex **1**,[31] with the only difference being a third Ce^{3+} in **7** and an extra OH^- (Table 2), as determined by BVS calculations and EPR spectroscopy. The $\{Ce_{24}O_{27}(OH)_9\}^{30+}$ core contains 21:3 versus 22:2 Ce^{4+}/Ce^{3+} in **1**, with the extra Ce^{3+} being assigned as Ce9 from its intermediate BVS value of 3.50; i.e., one Ce9 is Ce^{3+}, and its symmetry partner is Ce^{4+} (Table S7). The EPR spectrum for **7** shows more features than **1** consistent with interacting Ce^{3+} ions in close proximity (Figure S2). A total of 10 Ce^{4+} ions are 8-coordinate, 12 Ce^{4+} ions are 9-coordinate, and 2 Ce^{3+} ions are 10-coordinate. There are four μ_4-OH^- and five μ_3-OH^- ions on the surface, identified by BVS calculations: two of each type are found at each end of the molecule near the Ce^{3+} ions, and the ninth, O19, is in the middle and is identified by its BVS value of 1.65 (Table S8), intermediate between those for O^{2-} and OH^-, i.e., OH^- at one site and O^{2-} at its symmetry partner. The remaining ligation is provided by 30 $PhCO_2^-$ ligands and 4 terminal py ligands.

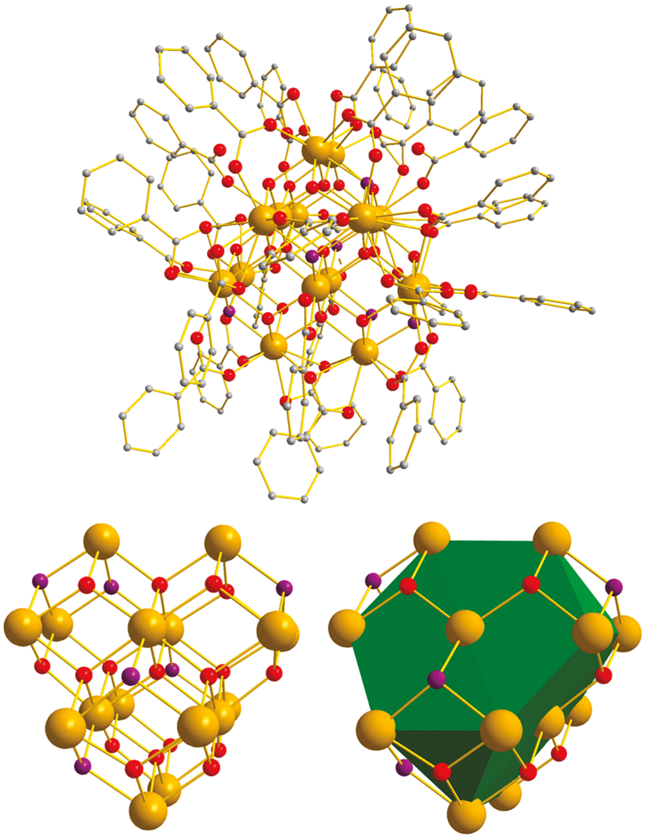

Figure 3. Full structure of complex **5** and its $\{Ce_{16}O_{17}(OH)_6\}^{24+}$ core. Color code: Ce^{4+}, gold; O, red; protonated O (i.e., OH^-), purple; C, gray; (111) facet, green. H atoms have been omitted for clarity.

Structural Comparison of Complexes 1−7. The previous study of **1**−**3**[31] had revealed structural features to atomic resolution, including the core size and morphology, surface facets, O-vacancy sites, location of Ce^{3+} and H^+ binding positions, and the organic ligand monolayer and its binding modes. Expansion of the family to **1**−**7** has now allowed the generality of earlier conclusions to be tested and any new features to be identified. An updated summary can now be provided:

(i) **1**−**7** have Ce_xO_y core diameters (largest O_{carb}−Ce···Ce−O_{carb} distance) from ~0.84 to ~1.93 nm (Figure 6) with Ce_xO_y core atom counts (excluding ligands) from Ce_6O_8 in **4** to $Ce_{40}O_{58}$ in **3**.

(ii) All exhibit the same fluorite structure as bulk CeO_2 (cubic Ce^{4+} and tetrahedral O^{2-} ions in the core body), with surface $Ce^{3+/4+}$ ions in various coordination environments, and,

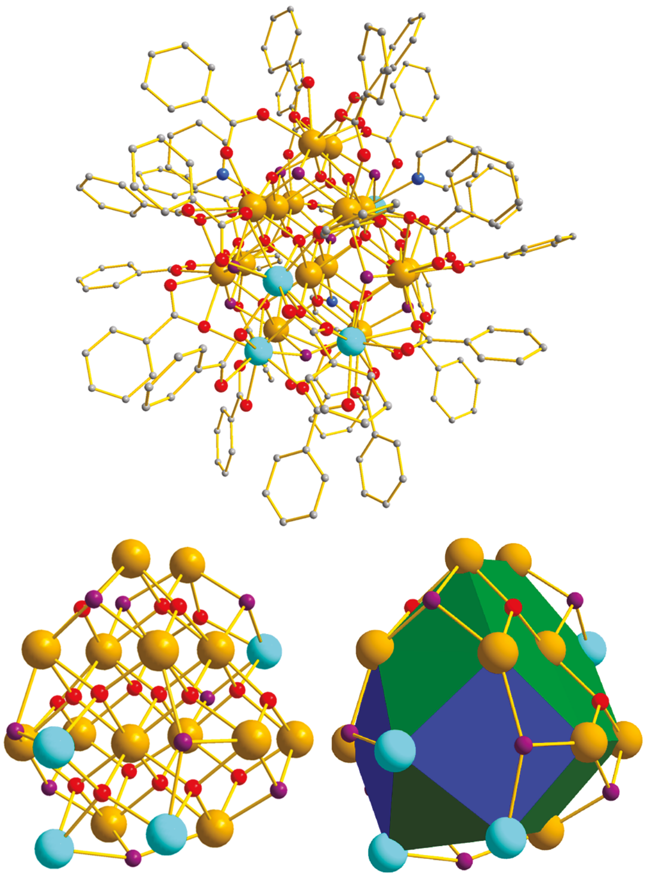

Figure 4. Full structure of complex **6** and its $\{Ce_{19}O_{18}(OH)_9\}^{27+}$ core. Color code: Ce^{4+}, gold; Ce^{3+}, sky blue; O, red; protonated O (i.e., OH^-), purple; C, gray; (111) facet, green; (100) facet, blue. H atoms have been omitted for clarity. The lone Ce^{3+} is atom Ce2.

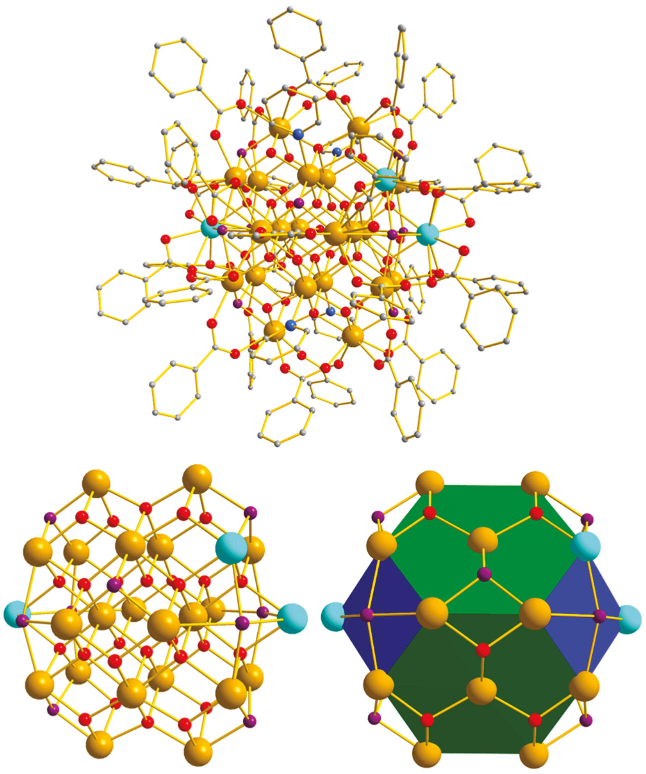

Figure 5. Full structure of complex **7** and its $\{Ce_{24}O_{27}(OH)_9\}^{30+}$ core. Color code: Ce^{4+}, gold; Ce^{3+}, sky blue; O, red; protonated O (i.e., OH^-), purple; C, gray; (111) facet, green; (100) facet, blue. H atoms have been omitted for clarity.

with the exception of very small **4** (<1 nm core), can thus be accurately described as “molecular nanoparticles” of CeO_2.

(iii) **1**, **3**, **6**, and **7** contain Ce^{3+} ions (Table 2), which are always on the surface coordinated to fewer O^{2-} ions than body Ce^{4+} ions, consistent with their lower charge.

(iv) They all display on their core surface the same low-index facets as those seen in CNPs (Figures 1−6), of which the (111) facets are known to be the most stable, i.e., lowest surface free energy. **4** is probably too small for this description to be applicable; nevertheless, **4** and **5** have only (111) facets, **1**, **2**, **6**, and **7** have (111) and (100) facets, and **3** has all three facets of (111), (100), and (110).

(v) Ce^{3+} ions in **1**−**3** were *always* found in a (100) Ce_4 square bridging two (100) facets into a V-shaped unit.[31] Now for the first time we see (100) facets containing two Ce^{3+} ions in **6** and **7**; in the former, there is also an unprecedented ${Ce^{3+}}_3$ triangle formed from three such (100) facets (Figures 4 and 5 and see below).

(vi) In addition to py capping (binding to the center of) of (111) hexagons, two new capping ligands have been seen in **4**−**7**, i.e., H_2O and RCO_2H (Figure 7a). An updated list of all ligand binding modes is given in Table 3.

(vii) Only four carboxylate binding modes were previously seen in **1**−**3** (Figure 7b−e), and **4**−**7** contain no new ones. We also previously identified that certain binding modes are found on certain facets or facet intersections (Figure S3), and a new example was found in **4**−**7**, the η^2:μ_2-chelating/bridging mode at the Ce_2 edge joining two intersecting (111) hexagonal facets in **5** and **6** (Table 3 and Figure S3d).

(viii) Yet another unprecedented observation is that in the triangle of (100) facets in **6** the μ_4-HO^- ions with rare tetragonal-pyramidal geometry—previously seen in **1**−**3** very weakly interacting with Ce_4 (100) squares (what we called “lids” on these facets)—are now μ_3 with T-shaped O geometry (Figures 4, 6, and 8a). We rationalize this as due to the distinct distortion in the shape and planarity of each Ce_4 square that this triangular arrangement causes in such a small cluster (Figure S5), allowing OH^- to form shorter, stronger interactions with just three Ce atoms, ignoring one of the Ce^{3+} ions ($Ce^{3+}\cdots OH^- \approx 3.5$ Å). This is supported by the O BVS values: μ_4-HO^- ions on a (100) Ce_4 facet have a BVS of 0.5−0.7 rather than the expected 1.0−1.2, reflecting the long contacts (∼2.7−3.0 Å) that are too long to be bonds; for comparison, Ce^{4+}−μ_3-O^{2-} = 2.2−2.3 Å, Ce^{4+}−μ_4-O^{2-} = 2.3−2.35 Å, and Ce^{4+}−μ_3-OH^- = 2.3−2.45 Å.[31] In the μ_3 T-shaped geometry, the OH^- ions give a larger BVS of 0.81−0.85 (Table S6) consistent with their now shorter (but still long) contacts of 2.4−2.65 Å (Table S9).

(ix) Also for the first time we see a Ce^{3+} not in a (100) facet, namely, Ce2 in Ce_{19} (**6**) located on the Ce2 edge joining two (111) hexagons (Figure 8b).

The picture that emerges from this summary is that many, but not all, of the trends observed previously for **1**−**3** still hold. The most common surface facet in **1**−**7** continues to be the (111) hexagon, which is consistent with the general consensus in the CNP literature that the (111) facet of CNPs is the most thermodynamically stable, followed by the (100) squares. Interestingly, the number of (100) facets is ∼$^1/_6$ the number of

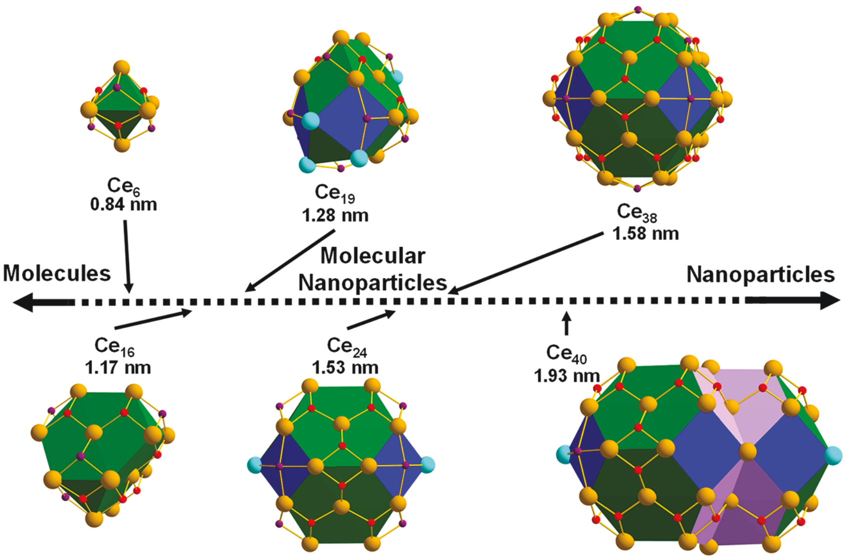

Figure 6. Cores of **1**−**7** with facets color coded, demonstrating their various sizes and Ce^{3+}/Ce^{4+} ratios. Color code: Ce^{4+}, gold; Ce^{3+}, sky blue; O, red; protonated O (i.e., OH^-), purple; (111) facet, green; (100) facet, blue; (110) facet, violet.

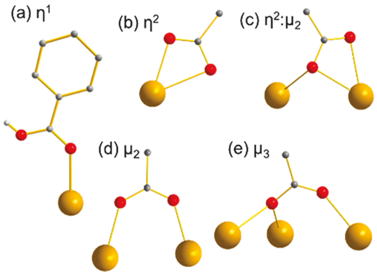

Figure 7. Complete set of (a) carboxylic acid and (b−e) carboxylate binding modes on the core surfaces of **1**−**7**.

Table 3. Surface Ligands and Their Binding Modes in 1−7

ligand	binding mode	found	surface location
O^{2-}	μ_3 bridging	**1**−**7**	(111) or (110) Ce_3 triangle
OH^-	μ_3 bridging[a]	**1**, **2**, **4**−**7**	(111) Ce_3 triangle
	μ_3 bridging[b]	**6**	lid on (100) Ce_4 square
OH^-	μ_4 bridging	1−3,7	lid on (100) Ce_4 square
py	terminal	**1**−**3**, **6**, **7**	capping of (111) hexagon
H_2O	terminal	**4**	capping Ce ions
		6	capping of (111) hexagon
RCO_2H	terminal	**5**	capping of (111) hexagon
MeCN	terminal	**3b**	lid on (100) Ce_4 square
RCO_2^-	η^2 chelating	**3**	lid on (100) Ce_4 square
RCO_2^-	η^2:μ_2 chelating/ bridging	**1**−**3**, **6**, **7**	Ce_2 edge joining (100) and (111)
		3	Ce_2 edge joining (110) and (111)
		5, **6**	Ce_2 edge joining (111) and (111)
RCO_2^-	μ_2 bridging	**1**−**7**	Ce_2 edge joining (111) and (111)
		3	Ce_2 edge joining (110) and (111)
RCO_2^-	μ_3 bridging	**3**	V-shaped Ce_3 edge of (110)

[a] Trigonal-pyramidal O geometry. [b] T-shaped O geometry.

Ce atoms (Table 3), except for the smallest, Ce_6 and Ce_{16}, which only have (111) hexagons and/or triangles. Ce_{40} (**3**) remains unique among **1**−**7** in having (110) facets (Figure 6).

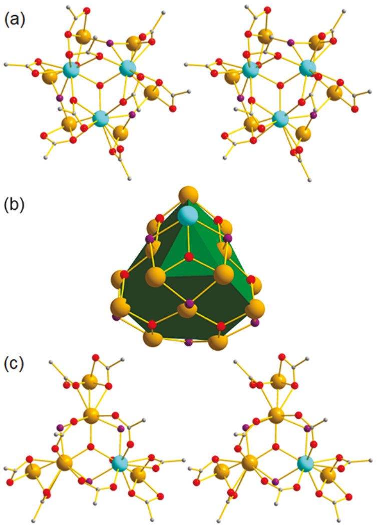

Figure 8. New surface structural features seen in **6**. (a) Stereopair of the triangle of three Ce^{3+} ions and three distorted (100) square facets seen at one end of the cluster. (b) Ce^{3+} at the other end of the molecule on the edge joining two (111) hexagonal facets. (c) Stereopair of the Ce_3 triangle at the same end as part b, showing the identical ligand environment of the Ce^{3+} and one Ce^{4+}. Color code: Ce^{4+}, gold; Ce^{3+}, sky blue; O, red; protonated O (i.e., OH^-), purple; (111) facet, green; (100) facet, blue.

The flexibility and versatility of carboxylates allow them to accommodate all surface features and degrees of curvature using a small number of bridging and/or chelating modes and as carboxylic acids even provide capping terminal ligands on (111) hexagons.

We were very interested in the triangle of Ce^{3+} and (100) squares in **6** because we had previously proposed weakly lidded Ce_4 sites as resting states of some of the catalytically highly reactive, surface O-vacancy sites in CNPs. Now, this unprecedented unit with its concentration of Ce^{3+} ions provides another potentially highly reactive site in small CNPs with points of high curvature, such as corners of cubes, octahedra, defect sites, and related structures, especially

https://dx.doi.org/10.1021/acs.inorgchem.0c03133
Inorg. Chem. 2021, 60, 1641−1653

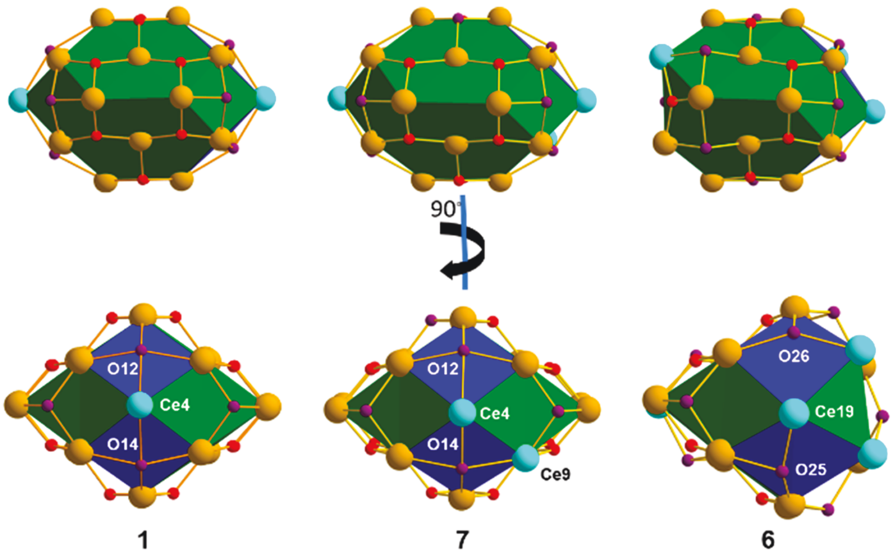

Figure 9. Cores of **1**, **6**, and **7** from two viewpoints showing how that of the Ce_{19} core of **6** is related to the Ce_{24} cores, as is the location of some of the Ce^{3+} ions in the clusters. Color code: Ce^{4+}, gold; Ce^{3+}, sky blue; O, red; protonated O (i.e., OH^-), purple; (111) facet, green; (100) facet, blue.

because its Ce^{3+} ions favor nearby accumulation of H^+ as OH^- ions (as was also seen previously in **1**/**3** and now in **6**/**7**; Figure 7a). Also particularly interesting is the observation for the first time of a Ce^{3+} in **6** that is not within a (100) square but instead on the edge at the intersection of two (111) hexagons (Figure 8b). In addition, given the virtual C_3 symmetry of the core, it was interesting that valence trapping of a Ce^{3+} was occurring at this one (Ce2) of three Ce atoms (Ce1−Ce3) equivalent by virtual core symmetry (Figure 8b,c). Valence trapping in **1** and **3** of Ce^{3+} at the intersection of two (100) Ce_4 squares had always made sense because this was a site with a smaller number of O^{2-} ions that favor Ce^{3+}, and the same applies to the triangular site in **6**. For atoms Ce1−Ce3, they are all attached to only $2O^{2-}$ and $2HO^-$ each, and the valence trapping of Ce^{3+} at Ce2 appears to be caused instead by more subtle factors: Ce1 is 8-coordinate, but both Ce2 and Ce3 are 9-coordinate with identical carboxylate binding modes (Figure 7c). This is another surprising aspect of **6**, and it is an important one because it provides the first unambiguous example in our work of Ce^{3+} and Ce^{4+} in *exactly* the same ligand environment, suggesting that such redox sites might be easier to redox cycle than others and thus of greater potential catalytic activity in redox chemistry. This also supports our assignment in **7**, which has a crystallographic inversion center of Ce9 as a Ce^{3+} at one site and a Ce^{4+} at its symmetry partner site on the basis of the BVS, as described above. We also note that the Ce_{19} core of **6** is structurally a fragment of the Ce_{24} cores of **1** and **7**, being obtained by the removal of five Ce from one end and one side of Ce_{24} (Figures 9 and S4 and Table S10). Also interesting is that one, two, and three of the Ce^{3+} ions in **1**, **7**, and **6**, respectively, are in related positions (Figure 9).

Catalytic Radical Scavenging by Molecular Nanoparticles. The advantages of molecular chemistry of monodispersity and crystallinity have allowed molecular nanoparticles **1**−**7** to be structurally characterized to atomic precision. This, in turn, now allows an investigation of their catalytic activity as a function of the size, Ce^{3+} content, and other parameters. As stated earlier, CNPs are widely used catalysts, but the polydispersity of samples, their range of the Ce^{3+}/Ce^{4+} content, etc., make definitive conclusions difficult to achieve. Are the molecular nanoparticles **1**−**7** even capable of catalysis like the larger CNPs, or are they too small? If they are capable, how does their activity compare with CNPs? To answer such questions, we have investigated the ability of **1**−**7** to catalytically scavenge ROS, namely hydroxyl radicals ($HO^\bullet$), an important test reaction of CNP catalytic activity in the <20 nm range in biomedical applications.[17,19,22,23]

To probe the hydroxyl radical scavenging ability in a controlled manner, EPR spectroscopy was employed to monitor spin-trapped hydroxyl radicals generated by the Fenton reaction by using the DMPO spin trap. The half-life of hydroxyl radicals in aqueous solution at room temperature is 10^{-9} s, but their reaction with nitrones or nitroso compounds generates longer-lived nitroxide radicals that can be detected, quantified, and monitored by EPR spectroscopy (Scheme 1).

Scheme 1. Reaction of a Hydroxyl Radical with the DMPO Spin Trap to Form the DMPO/OH$^\bullet$ Adduct

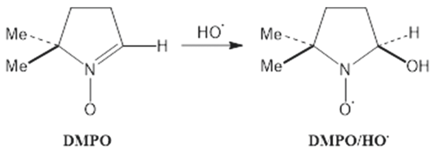

The DMPO/HO$^\bullet$ adduct gives a characteristic four-line EPR signal with a 1:2:2:1 ratio from the hyperfine coupling of the unpaired electron with the ^{14}N and 2-^1H nuclei, and $a_N = a_H =$ 14.9 G.

The catalytic scavenging activity was assessed by monitoring the EPR signal of the DMPO/HO$^\bullet$ adduct in the absence (control) and presence of **1**−**7**. If the molecular nanoparticles are excellent scavengers of $HO^\bullet$, they will efficiently compete with DMPO and reduce the amount of the DMPO/HO$^\bullet$ adduct that is formed and thus the intensity of the EPR signal detected. As a control, we first investigated whether any significant DMPO/HO$^\bullet$ signal is generated if Fe^{2+} is not added, i.e., if the molecular nanoparticles themselves can decompose H_2O_2 to $HO^\bullet$, but in all cases we observed only very weak signals even after several minutes, <1% of those generated with Fe^{2+} in the absence of **1**−**7** (control for the scavenging studies). Because $FeCl_2$ is added just a few seconds after the other reagents, we therefore assume that the same initial hydroxyl radical concentration is produced with and without **1**−**7** being present. EPR spectra were recorded every minute for the Fenton reaction in the absence (control) or presence of 1 mM molecular nanoparticle (**1**−**7**), and the intensity of the second line at 3507 G in the four-line spectrum was plotted versus time, with many of the molecular nanoparticles reaching their asymptotic state well before monitoring stopped. The results were normalized to the control being intensity 1.0 and are plotted in Figure 10.

The first important observation is that almost all of the complexes can efficiently scavenge $HO^\bullet$ radicals, as indicated by significantly weakened or near-absent signals of the DMPO/$HO^\bullet$ adduct relative to the control, even after just 1 min (Figure 10a). Note that assuming stoichiometric formation of $HO^\bullet$ from the available H_2O_2 means that there is a greater than 1 order of magnitude excess over DMPO. For **1**, **2**, and **4**, the intensity of the adduct signal was almost zero within 1 min, indicating that the clusters had scavenged $HO^\bullet$ so efficiently that almost no spin-trap adduct could be formed. **3** and **5** were only a little less efficient, but **6** and **7** were relatively poor radical scavengers. For comparison, the first three spectra for **4** and **7** are shown in Figure 10b,c. **1**−**5** are thus all exhibiting a dramatic increase in the scavenging efficiency compared to CNPs at the ≤20 nm size regime previously investigated by analogous EPR spin-trap techniques:[44,45] For example, 18 nm CNPs decrease the half-life of the DMPO/$HO^\bullet$ adduct from 960 to 747 s, whereas for **1**−**5**, the half-life is less than 60 s.[20] Similarly, Babu et al. monitored the radical scavenging ability by EPR of 3−5 nm CNPs at 1 mM and 10 μM concentrations, showing a decrease in the decay constant for catalysis at 10 μM from 19.4 to 7.4 min (Figure S6);[44] interestingly, there was little effect at 1 mM, which was assigned to agglomeration of the CNPs.

Filippi et al. suggested that an observed decrease of the spin-trapped $HO^\bullet$ signal in the presence of CNPs could, in principle, be due to a number of different processes: (i) surface adsorption of H_2O_2, (ii) catalase-like behavior, and (iii) $HO^\bullet$ radical scavenging.[46] We thus considered which of these possibilities could rationalize the decrease in the EPR signal of spin-trapped $HO^\bullet$ that we observed with our molecular nanoparticles. For part i, Baldim et al. calculated that CNPs of diameter 4.5−28 nm were able to adsorb 2−17 H_2O_2 molecules per square nanometers, depending on both the CNP and the surface area of the CNP.[47] Because each of the molecular nanoparticles **1**−**7** has a small surface area and an organic monolayer, it seems unlikely that this process would cause an appreciable decrease in H_2O_2 and therefore decrease the total $HO^\bullet$ generated. For part ii, catalase-like disproportionation of H_2O_2 would result in the formation of O_2 and H_2O, and therefore fewer $HO^\bullet$ radicals. The decomposition rate of H_2O_2 in a catalase-like behavior has been estimated to be ∼2.7 nmol min^{-1} for CNPs containing ∼70% Ce^{4+}.[48] Applying this decomposition rate suggests that during the course of our radical scavenging experiments <0.1% of H_2O_2 was lost to catalase-like disproportionation by Ce/O molecular nanoparticles **1**−**7**. This decomposition rate may be slightly greater for **1**−**7** because of the greater concentration of Ce^{4+} ions, but it is unlikely that it would explain a significant decrease in H_2O_2. Therefore, we conclude that the observed decrease in the EPR signal intensity is indeed due to the scavenging of $HO^\bullet$ radicals by the Ce/O molecular nanoparticles. **1**−**5** thus show much higher activities than CNPs, which we rationalize as being due to a combination of their small size, resulting in a large surface-area-to-volume ratio, and protection from agglomeration by the surface RCO_2^- monolayer. The importance of the latter point should not be underestimated: the use of small carboxylates, rather than oleic acid or similar long-chain acid or amine surfactants used in the synthesis of CNPs, gives an organic monolayer that is thick enough to

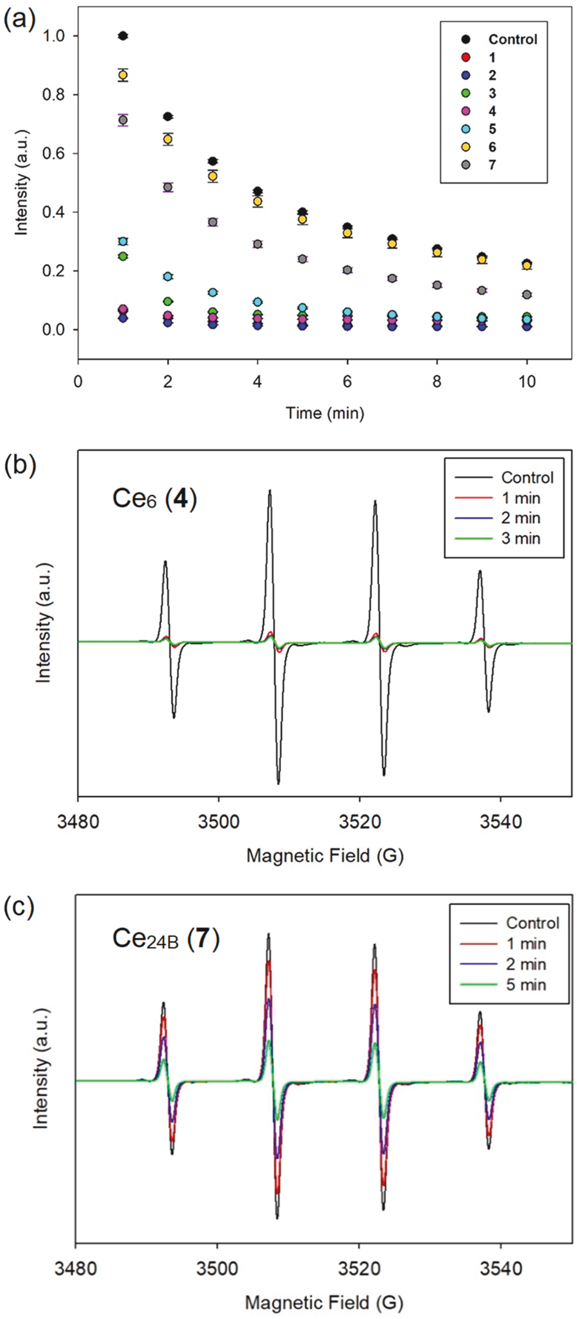

Figure 10. $HO^\bullet$ scavenging by molecular nanoparticles **1**−**7**. (a) Plots of the EPR signal intensity versus time of the second peak at ∼3507 G of the DMPO/$HO^\bullet$ adduct from the reaction of H_2O_2 (10 mM), $FeCl_2$(10 mM), and DMPO (0.5 M) in the absence (control) and presence of 1 mM **1**−**7**. (b) First three EPR spectra of the DMPO/$HO^\bullet$ adduct generated from the reaction in the absence (control) and presence of 1 mM **4** (Ce_6). (c) Same as that for part b but using 1 mM **3** (Ce_{40}).

prevent agglomeration of the molecular nanoparticles but thin enough to not prevent access to the surface and require its removal.

Complexes **1**, **2**, **4**, and **5** vary significantly in size (0.84–1.58 nm), and the next conclusion to be drawn from Figure 10a is that the catalytic activity of molecular nanoparticles in this ultrasmall nanoscale regime does not correlate with the particle size, i.e., metal nuclearity. The activity also does not correlate with the carboxylate identity; otherwise, **1** and **5**–**7** would all have similar activities. Other factors must be in play. When the data are separated into two plots, one for complexes containing Ce^{3+} ions (Figure 11a) and the other for those with only Ce^{4+} ions (Figure 11b), a clearer correlation emerges: For the former, the higher is the Ce^{3+} content, the lower is the resultant scavenging ability; thus, **1**/**3** ($2Ce^{3+}$) > **7** ($3Ce^{3+}$) > **6** ($4Ce^{3+}$). For the latter, clusters that only contain Ce^{4+} are efficient scavengers, regardless of the size. It would thus appear that a major factor determining the radical scavenging activity is the surface concentration of Ce^{3+}, but how the presence of Ce^{3+} inhibits $HO^\bullet$ scavenging is not clear. Other questions also spring to mind, but the limited number of available clusters make it difficult to answer them unequivocally at the present time. For example, is the difference between **1** and **3** simply because of the greater "concentration" of Ce^{3+} (i.e., Ce^{3+}/Ce^{4+} ratio), and/or the presence in **3** of the (110) facets, or some other factor? Similarly, is the slightly lower activity of **5** versus **2**/**4** due to another factor such as the absence of surface (100) facets? Further, is it just the higher total Ce^{3+} in **6** and **7** that makes them poor scavengers or the fact that this allows them to contain two and three Ce^{3+}, respectively, in close proximity, unlike **1** and **3**, where the two Ce^{3+} ions are at opposite ends?

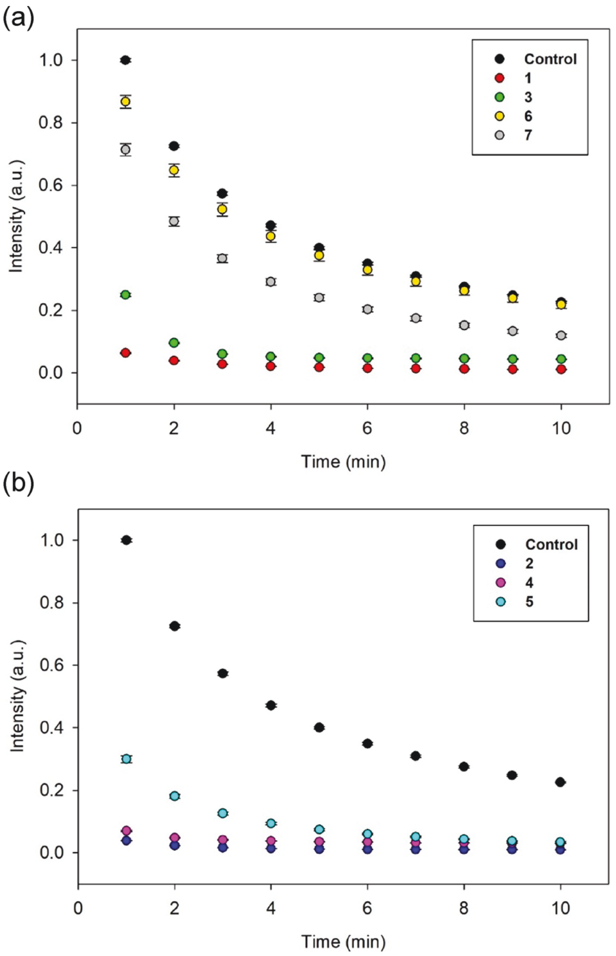

Figure 11. Same as Figure 10a but separated into (a) complexes that contain Ce^{3+}/Ce^{4+} ions and (b) complexes that contain only Ce^{4+} ions.

A comparison of our results on **1**–**7** with those in the CNP literature is complicated by the polydispersity and range of the Ce^{3+}/Ce^{4+} ratios in CNP samples. In general, a high Ce^{3+}/Ce^{4+} ratio is typically considered to be beneficial for $HO^\bullet$ radical scavenging, in contrast to our own results, but Filippi et al. have also observed efficient $HO^\bullet$ radical scavenging by CNPs with low Ce^{3+} concentrations.[46] Similarly, in a kinetic model developed by Reed et al., it was shown that Ce^{4+} could effectively scavenge $O_2^{-\bullet}$, which like $HO^\bullet$ scavenging is typically also considered to be favored by high Ce^{3+}/Ce^{4+} ratios.[49] It is thus difficult to come to firm conclusions by comparing our results with these and others in the literature.

Because the surface facet composition was mentioned above as a possible factor in determining the scavenging ability, we note that this has been explored with CNPs. For example, Zhang et al. studied the scavenging ability of different morphologies and attributed the higher activity of nanowires and nanorods to their higher exposure of (100) and (110) facets than nanoparticles;[50] the recognized activity order for CNPs is (100) ≥ (110) > (111) due to the low formation energy of O vacancies in (100) and (110) facets and thus Ce^{3+} locations, allowing for efficient Ce^{3+}/Ce^{4+} cycling.[1,2] The size of the particles and Ce^{3+} concentration were concluded to be similar for all morphologies and therefore did not contribute to the differences in the scavenging ability.

For **1**–**7**, they all display some (100) facets except **4** and **5**, which display only (111) facets (Table 1), and, in addition to both the (100) and (111) facets, **3** displays (110) facets. The presence of (100) facets may be contributing to some of the observed activity differences; namely, **2** is all-Ce^{4+} with six (100) facets and efficiently scavenges radicals, whereas **5** is also all-Ce^{4+} but only possesses (111) facets and scavenges radicals less efficiently. However, **2** exhibits reactivity almost identical with that of **4**. We conclude that at best we see a small facet dependence at this ultrasmall size regime and for the limited number of clusters available for study to date.

Agglomeration of CNPs is another factor that affects their radical scavenging activity,[51] but the organic monolayer in **1**-**7** should prevent this. We thus investigated the effect of concentration on scavenging ability for **1**, **3** and **7** (Figure 12); **1** and **7** were chosen since they only vary in Ce^{3+}/Ce^{4+} ratio but show very different scavenging ability and are not water-soluble. **3** was chosen since it is fully water-soluble. For **1** and **3**, even the small increases in concentration lead to noticeable increases in radical scavenging, in contrast to CNPs where, for example, increases of the concentration by a factor up to 400 were reported to lead to decreasing relative activity assigned to agglomeration.[45] This indicates that significant agglomeration for molecular nanoparticles is unlikely, as the relative surface area would not be linear with respect to concentration. For **7**, since it is not an effective radical scavenger, there are almost no differences in scavenging ability by varying the concentration.

The use of ≤20 nm CNPs in medical applications must address toxicity side effects, including from particle agglomeration and a prooxidant (radical-generating) ability of CNPs; for the latter behavior, the particle size, shape, surface charge,

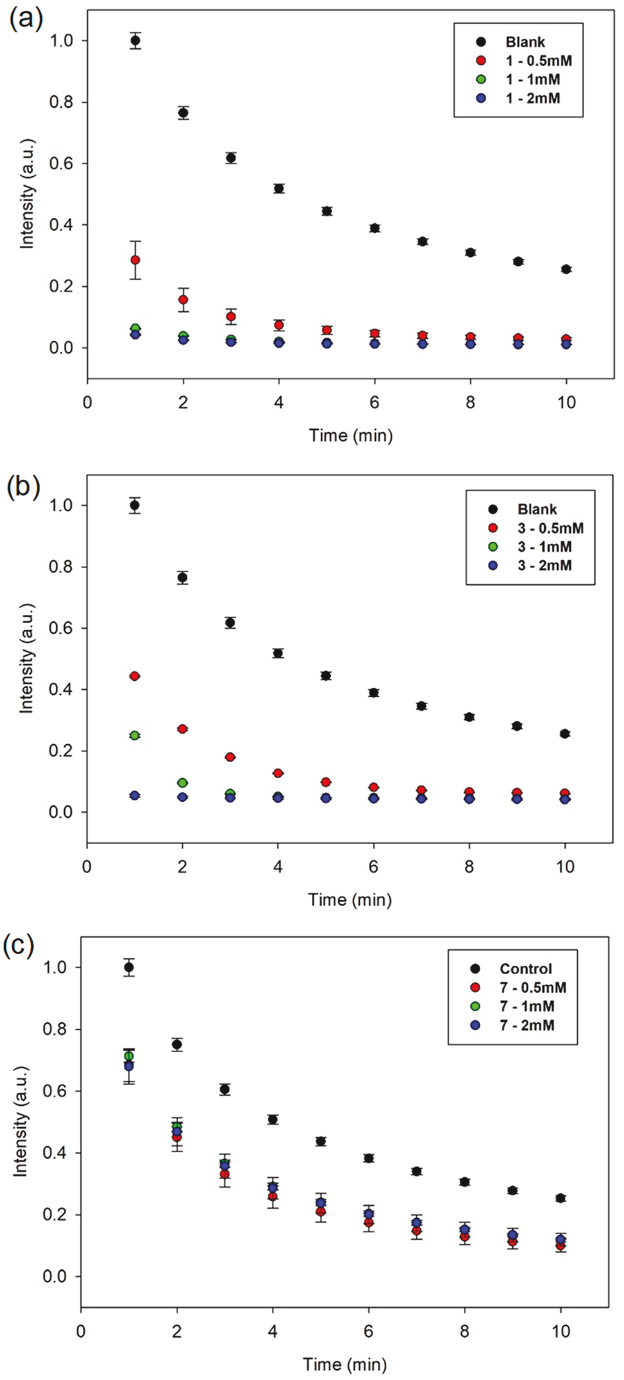

Figure 12. Intensity versus time plot of the DMPO spin-trap adduct EPR signal in the absence (blank) and presence of complexes (a) **1**, (b) **7**, and (c) **3** in concentrations of 0.5, 1, and 2 mM.

Ce^{3+}/Ce^{4+} ratio, and others have been suggested as possible causes for this CNP toxicity.[29,52−55] However, because of the difficulty in controlling these properties, exact variables that promote prooxidant versus antioxidant activity by CNPs have not been fully established. As mentioned above, control experiments exploring whether **1**−**7** in the absence of Fe^{2+} also possess radical-generating ability gave only trace DMPO/$HO^{\bullet}$ adduct signals, which indicates that, under the present conditions at least, they have very poor prooxidant activity, and thus it is difficult to draw any correlations with the size or Ce^{3+} content.

On the basis of all of the above results, we can summarize our observations, which represent working hypotheses for future studies as we aim to increase the limited number of compounds available: (i) in the presence of Fe^{2+} generating large amounts of $HO^{\bullet}$ from the Fenton reaction, most of the molecular nanoparticles **1**−**7** exhibit excellent radical scavenging activity, with the main correlation being that the activity is inversely related to the Ce^{3+} content. (ii) In the absence of Fe, **1**−**7** exhibit very weak prooxidant activity difficult to correlate with their relative structural and redox features.

■ CONCLUSIONS

Our family of molecular nanoparticles that represents a bottom-up molecular route to ultrasmall nanoparticles of CeO_2 has been expanded with the addition of Ce_6 (**4**), Ce_{16} (**5**), Ce_{19} (**6**), and Ce_{24B} (**7**). They are all of equal or smaller nuclearity than **1**−**3** and display various Ce^{3+}/Ce^{4+} ratios and some interesting surface features not seen previously, especially **6** with its high Ce^{3+} content, new structural features, and similarity to **1** and **7**. Overall, the expanded family now provides a wealth of structural details on ultrasmall nanoparticles of <2 nm size and further supports our conclusion that the μ_3- or μ_4-OH^- groups that are lids on (100) Ce_4 squares represent sites of increased reactivity and possible "O-vacancy" sites. The focus is now on extending the family to higher nuclearities than **3** (Ce_{40}), and such efforts are in progress.

1−**5** exhibit very high catalytic ROS scavenging activity at room temperature, showing that they are not "too small" to be good catalysts. The observed trend that the activity decreases with the Ce^{3+} content is in contrast to many (but not all) results in the CNP literature and may merely reflect the ultrasmall size of **1**−**7**, which, for example, means that their Ce ions are all or nearly all on the surface. This may preclude the influence, including O mobility, of the body atoms of larger CNPs on the surface reactivity, and, in fact, such a size effect on O mobility in the regeneration of antioxidant activity has been reported in CNPs in the 2−10 nm range.[56] We may thus be "comparing apples with oranges" when we compare our results with most of those in the CNP literature. The Ce^{3+}/Ce^{4+} ratio in **1**−**7** shows the most obvious correlation with activity, but other factors are clearly also important to some extent, and it will take an even larger family of compounds to map these out, including higher nuclearities. The surprising differences between isostructural **1** and **7** show that simple redox cycling cannot be the mechanism of scavenging, which remains unclear also for CNPs. At their size and for $OH^{\bullet}$ scavenging at least, it is the all-Ce^{4+} molecular nanoparticles that have the highest activity. It will be interesting to see what activity higher-nuclearity members than **1**−**7** will exhibit. We shall also investigate whether the same inverse correlation of activity with the Ce^{3+} content holds in the scavenging of other ROS such as superoxide.

■ ASSOCIATED CONTENT

SI Supporting Information

The Supporting Information is available free of charge at https://pubs.acs.org/doi/10.1021/acs.inorgchem.0c03133.

Ce and O BVS tables, structural figures, and EPR spectra for **6** and **7** (PDF)

Accession Codes

CCDC 2024106–2024109 contain the supplementary crystallographic data for this paper. These data can be obtained free of charge via www.ccdc.cam.ac.uk/data_request/cif, or by emailing data_request@ccdc.cam.ac.uk, or by contacting The Cambridge Crystallographic Data Centre, 12 Union Road, Cambridge CB2 1EZ, UK; fax: +44 1223 336033.

AUTHOR INFORMATION

Corresponding Author

George Christou – *Department of Chemistry, University of Florida, Gainesville, Florida 32611-7200, United States;* orcid.org/0000-0001-5923-5523; Phone: +1-352-392-8314; Email: christou@chem.ufl.edu

Authors

Kylie J. Mitchell – *Department of Chemistry, University of Florida, Gainesville, Florida 32611-7200, United States*

Justin L. Goodsell – *Department of Chemistry, University of Florida, Gainesville, Florida 32611-7200, United States*

Bradley Russell-Webster – *Department of Chemistry, University of Florida, Gainesville, Florida 32611-7200, United States*

Umar T. Twahir – *Department of Chemistry, University of Florida, Gainesville, Florida 32611-7200, United States*

Alexander Angerhofer – *Department of Chemistry, University of Florida, Gainesville, Florida 32611-7200, United States;* orcid.org/0000-0002-8580-6024

Khalil A. Abboud – *Department of Chemistry, University of Florida, Gainesville, Florida 32611-7200, United States*

Complete contact information is available at:
https://pubs.acs.org/10.1021/acs.inorgchem.0c03133

Notes

The authors declare no competing financial interest.

ACKNOWLEDGMENTS

We thank the National Science Foundation (NSF) for support of this work (Grant CHE-1900321). We also thank the NSF for funding of the X-ray diffractometer through Grant CHE-1828064.

REFERENCES

(1) Flytzani-Stephanopoulos, M. Nanostructured Cerium Oxide "Ecocatalysts. *MRS Bull.* **2001**, *26*, 885–889.

(2) Trovarelli, A. Catalytic Properties of Ceria and CeO2-Containing Materials. *Catal. Rev.: Sci. Eng.* **1996**, *38*, 439–520.

(3) Sun, C.; Li, H.; Chen, L. Nanostructured Ceria-Based Materials: Synthesis, Properties, and Applications. *Energy Environ. Sci.* **2012**, *5*, 8475–8505.

(4) Reed, K.; Cormack, A.; Kulkarni, A.; Mayton, M.; Sayle, D.; Klaessig, F.; Stadler, B. Exploring the Properties and Applications of Nanoceria: Is There Still Plenty of Room at the Bottom? *Environ. Sci.: Nano* **2014**, *1*, 390–405.

(5) Murray, E. P.; Tsai, T.; Barnett, S. A. A Direct-Methane Fuel Cell with a Ceria-Based Anode. *Nature* **1999**, *400*, 649–651.

(6) Kharton, V. V.; Figueiredo, F. M.; Navarro, L.; Naumovich, E. N.; Kovalevsky, A. V.; Yaremchenko, A. A.; Viskup, A. P.; Carneiro, A.; Marques, F. M. B.; Frade, J. R. Ceria-Based Materials for Solid Oxide Fuel Cells. *J. Mater. Sci.* **2001**, *36*, 1105–1117.

(7) Perullini, M.; Bilmes, S.; Jobbagy, M.; Brayner, R.; Fievet, F.; Coradin, T. Cerium Oxide Nanoparticles: Structure, Applications, Reactivity, and Eco-Toxicology. *Nanomaterials: A Danger or a Promise?*; Springer: London, 2012; pp 307–334.

(8) Wu, Z.; Li, M.; Overbury, S. H. On the Structure Dependence of CO Oxidation over CeO_2 Nanocrystals with Well-Defined Surface Planes. *J. Catal.* **2012**, *285*, 61–73.

(9) Ma, Y.; Gao, W.; Zhang, Z.; Zhang, S.; Tian, Z.; Liu, Y.; Ho, J. C.; Qu, Y. Regulating the Surface of Nanoceria and Its Applications in Heterogeneous Catalysis. *Surf. Sci. Rep.* **2018**, *73*, 1–36.

(10) Sharma, S.; Hu, Z.; Zhang, P.; McFarland, E. W.; Metiu, H. CO_2 Methanation on Ru-Doped Ceria. *J. Catal.* **2011**, *278*, 297–309.

(11) Grirrane, A.; Corma, A.; García, H. Gold-Catalyzed Synthesis of Aromatic Azo Compounds from Anilines and Nitroaromatics. *Science* **2008**, *322*, 1661–1664.

(12) Chueh, W. C.; Haile, S. M. Ceria as a Thermochemical Reaction Medium for Selectively Generating Syngas or Methane from H_2O and CO_2. *ChemSusChem* **2009**, *2*, 735–739.

(13) Zhang, P.; Lu, H.; Zhou, Y.; Zhang, L.; Wu, Z.; Yang, S.; Shi, H.; Zhu, Q.; Chen, Y.; Dai, S. Mesoporous $MnCeO_x$ Solid Solutions for Low Temperature and Selective Oxidation of Hydrocarbons. *Nat. Commun.* **2015**, *6*, 8446.

(14) Carrettin, S.; Concepción, P.; Corma, A.; López Nieto, J. M.; Puntes, V. F. Nanocrystalline CeO_2 Increases the Activity of Au for CO Oxidation by Two Orders of Magnitude. *Angew. Chem., Int. Ed.* **2004**, *43*, 2538–2540.

(15) Tabakova, T.; Boccuzzi, F.; Manzoli, M.; Sobczak, J. W.; Idakiev, V.; Andreeva, D. A Comparative Study of Nanosized IB/Ceria Catalysts for Low-Temperature Water-Gas Shift Reaction. *Appl. Catal., A* **2006**, *298*, 127–143.

(16) Lee, S. S.; Song, W.; Cho, M.; Puppala, H. L.; Nguyen, P.; Zhu, H.; Segatori, L.; Colvin, V. L. Antioxidant Properties of Cerium Oxide Nanocrystals as a Function of Nanocrystal Diameter and Surface Coating. *ACS Nano* **2013**, *7*, 9693–9703.

(17) Das, S.; Dowding, J. M.; Klump, K. E.; McGinnis, J. F.; Self, W.; Seal, S. Cerium Oxide Nanoparticles: Applications and Prospects in Nanomedicine. *Nanomedicine* **2013**, *8*, 1483–1508.

(18) Walkey, C.; Das, S.; Seal, S.; Erlichman, J.; Heckman, K.; Ghibelli, L.; Traversa, E.; McGinnis, J. F.; Self, W. T. Catalytic Properties and Biomedical Applications of Cerium Oxide Nanoparticles. *Environ. Sci.: Nano* **2015**, *2*, 33–53.

(19) Xu, C.; Qu, X. Cerium Oxide Nanoparticle: A Remarkably Versatile Rare Earth Nanomaterial for Biological Applications. *NPG Asia Mater.* **2014**, *6*, No. e90.

(20) Spulber, M.; Baumann, P.; Liu, J.; Palivan, C. G. Ceria Loaded Nanoreactors: A Nontoxic Superantioxidant System with High Stability and Efficacy. *Nanoscale* **2015**, *7*, 1411–1423.

(21) Bhushan, B.; Nandhagopal, S.; Rajesh Kannan, R.; Gopinath, P. Biomimetic Nanomaterials: Development of Protein Coated Nanoceria as a Potential Antioxidative Nano-Agent for the Effective Scavenging of Reactive Oxygen Species in Vitro and in Zebrafish Model. *Colloids Surf., B* **2016**, *146*, 375–386.

(22) Nelson, B. C.; Johnson, M. E.; Walker, M. L.; Riley, K. R.; Sims, C. M. Antioxidant Cerium Oxide Nanoparticles in Biology and Medicine. *Antioxidants* **2016**, *5*, 15.

(23) Pulido-Reyes, G.; Rodea-Palomares, I.; Das, S.; Sakthivel, T. S.; Leganes, F.; Rosal, R.; Seal, S.; Fernández-Piñas, F. Untangling the Biological Effects of Cerium Oxide Nanoparticles: The Role of Surface Valence States. *Sci. Rep.* **2015**, *5*, No. srep15613.

(24) Ouyang, Z.; Mainali, M. K.; Sinha, N.; Strack, G.; Altundal, Y.; Hao, Y.; Winningham, T. A.; Sajo, E.; Celli, J.; Ngwa, W. Potential of Using Cerium Oxide Nanoparticles for Protecting Healthy Tissue during Accelerated Partial Breast Irradiation (APBI). *Physica Medica* **2016**, *32*, 631–635.

(25) Celardo, I.; Pedersen, J. Z.; Traversa, E.; Ghibelli, L. Pharmacological Potential of Cerium Oxide Nanoparticles. *Nanoscale* **2011**, *3*, 1411–1420.

(26) Winkler, B. S.; Orselli, S. M.; Rex, T. S. The Redox Couple between Glutathione and Ascorbic Acid: A Chemical and Physiological Perspective. *Free Radical Biol. Med.* **1994**, *17*, 333–349.

(27) Xue, Y.; Luan, Q.; Yang, D.; Yao, X.; Zhou, K. Direct Evidence for Hydroxyl Radical Scavenging Activity of Cerium Oxide Nanoparticles. *J. Phys. Chem. C* **2011**, *115*, 4433–4438.

(28) Lu, M.; Zhang, Y.; Wang, Y.; Jiang, M.; Yao, X. Insight into Several Factors That Affect the Conversion between Antioxidant and Oxidant Activities of Nanoceria. *ACS Appl. Mater. Interfaces* **2016**, *8*, 23580−23590.

(29) Dowding, J. M.; Das, S.; Kumar, A.; Dosani, T.; McCormack, R.; Gupta, A.; Sayle, T. X. T.; Sayle, D. C.; von Kalm, L.; Seal, S.; Self, W. T. Cellular Interaction and Toxicity Depend on Physicochemical Properties and Surface Modification of Redox-Active Nanomaterials. *ACS Nano* **2013**, *7*, 4855−4868.

(30) Asati, A.; Santra, S.; Kaittanis, C.; Nath, S.; Perez, J. M. Oxidase-Like Activity of Polymer-Coated Cerium Oxide Nanoparticles. *Angew. Chem., Int. Ed.* **2009**, *48*, 2308−2312.

(31) Mitchell, K. J.; Abboud, K. A.; Christou, G. Atomically-Precise Colloidal Nanoparticles of Cerium Dioxide. *Nat. Commun.* **2017**, *8*, 1445.

(32) Russell-Webster, B.; Abboud, K. A.; Christou, G. Molecular Nanoparticles of Cerium Dioxide: Structure-Directing Effect of Halide Ions. *Chem. Commun.* **2020**, *56*, 5382−5385.

(33) *SAINT*; Bruker AXS: Madison, WI, 2013.

(34) Sheldrick, G. *SHELXTL2013*; Bruker AXS, Madison, WI, 2013.

(35) Sheldrick, G. *SHELXTL2014*; Bruker AXS, Madison, WI, 2014.

(36) *SQUEEZE*: van der Sluis, P.; Spek, A. L. P. BYPASS: an effective method for the refinement of crystal structures containing disordered solvent regions. *Acta Crystallogr., Sect. A: Found. Crystallogr.* **1990**, *46*, 194−201.

(37) *PLATON*: Spek, A. L. Structure validation in chemical crystallography. *Acta Crystallogr., Sect. D: Biol. Crystallogr.* **2009**, *65*, 148−155.

(38) Mereacre, V.; Ako, A. M.; Akhtar, M. N.; Lindemann, A.; Anson, C. E.; Powell, A. K. Homo- and Heterovalent Polynuclear Cerium and Cerium/Manganese Aggregates. *Helv. Chim. Acta* **2009**, *92*, 2507−2524.

(39) Brown, I. D. Recent Developments in the Methods and Applications of the Bond Valence Model. *Chem. Rev.* **2009**, *109*, 6858−6919.

(40) (a) Estes, S. L.; Antonio, M. R.; Soderholm, L. Tetravalent Ce in the Nitrate-Decorated Hexanuclear Cluster $[Ce_6(\mu_3\text{-}O)_4(\mu_3\text{-}OH)_4]^{12+}$: A Structural End Point for Ceria Nanoparticles. *J. Phys. Chem. C* **2016**, *120*, 5810−5818. (b) Hennig, C.; Ikeda-Ohno, A.; Kraus, W.; Weiss, S.; Pattison, P.; Emerich, H.; Abdala, P. M.; Scheinost, A. C. Crystal Structure and Solution Species of Ce(III) and Ce(IV) Formates: From Mononuclear to Hexanuclear Complexes. *Inorg. Chem.* **2013**, *52*, 11734−11743.

(41) (a) Das, R.; Sarma, R.; Baruah, J. B. A Hexanuclear Cerium(IV) Cluster with Mixed Coordination Environment. *Inorg. Chem. Commun.* **2010**, *13*, 793−795. (b) Mathey, L.; Paul, M.; Copéret, C.; Tsurugi, H.; Mashima, K. Cerium(IV) Hexanuclear Clusters from Cerium(III) Precursors: Molecular Models for Oxidative Growth of Ceria Nanoparticles. *Chem. - Eur. J.* **2015**, *21*, 13454−13461.

(42) Malaestean, I. L.; Ellern, A.; Baca, S.; Kogerler, P. Cerium oxide nanoclusters: commensurate with concepts of polyoxometalate chemistry? *Chem. Commun.* **2012**, *48*, 1499−1501.

(43) Wasson, M. C.; Zhang, X.; Otake, K.; Rosen, A. S.; Alayoglu, S.; Krzyaniak, M. D.; Chen, Z.; Redfern, L. R.; Robison, L.; Son, F. A.; Chen, Y.; Islamoglu, T.; Notestein, J. M.; Snurr, R. Q.; Wasielewski, M. R.; Farha, O. K. Supramolecular Porous Assemblies of Atomically Precise Catalytically Active Cerium-Based Clusters. *Chem. Mater.* **2020**, *32* (19), 8522−8529.

(44) Babu, S.; Velez, A.; Wozniak, K.; Szydlowska, J.; Seal, S. Electron Paramagnetic Study on Radical Scavenging Properties of Ceria Nanoparticles. *Chem. Phys. Lett.* **2007**, *442*, 405−408.

(45) Schlick, S.; Danilczuk, M.; Drews, A. R.; Kukreja, R. S. Scavenging of Hydroxyl Radicals by Ceria Nanoparticles: Effect of Particle Size and Concentration. *J. Phys. Chem. C* **2016**, *120*, 6885−6890.

(46) Filippi, A.; Liu, F.; Wilson, J.; Lelieveld, S.; Korschelt, K.; Wang, T.; Wang, Y.; Reich, T.; Pöschl, U.; Tremel, W.; Tong, H. Antioxidant Activity of Cerium Dioxide Nanoparticles and Nanorods in Scavenging Hydroxyl Radicals. *RSC Adv.* **2019**, *9*, 11077−11081.

(47) Baldim, V.; Bedioui, F.; Mignet, N.; Margaill, I.; Berret, J.-F. The Enzyme-like Catalytic Activity of Cerium Oxide Nanoparticles and Its Dependency on Ce^{3+} Surface Area Concentration. *Nanoscale* **2018**, *10*, 6971−6980.

(48) Pirmohamed, T.; Dowding, J. M.; Singh, S.; Wasserman, B.; Heckert, E.; Karakoti, A. S.; King, J. E. S.; Seal, S.; Self, W. T. Nanoceria Exhibit Redox State-Dependent Catalase Mimetic Activity. *Chem. Commun.* **2010**, *46*, 2736−2738.

(49) Reed, K.; Bush, N.; Burns, Z.; Doherty, G.; Foley, T.; Milone, M.; Maki, K. L.; Cromer, M. Modeling the Kinetic Behavior of Reactive Oxygen Species with Cerium Dioxide Nanoparticles. *Biomolecules* **2019**, *9*, 447.

(50) Zhang, Y.; Zhou, K.; Zhai, Y.; Qin, F.; Pan, L.; Yao, X. Crystal Plane Effects of Nano-CeO_2 on Its Antioxidant Activity. *RSC Adv.* **2014**, *4*, 50325−50330.

(51) Grulke, E.; Reed, K.; Beck, M.; Huang, X.; Cormack, A.; Seal, S. Nanoceria: Factors Affecting Its pro- and Anti-Oxidant Properties. *Environ. Sci.: Nano* **2014**, *1*, 429−444.

(52) Asati, A.; Santra, S.; Kaittanis, C.; Perez, J. M. Surface-Charge-Dependent Cell Localization and Cytotoxicity of Cerium Oxide Nanoparticles. *ACS Nano* **2010**, *4*, 5321−5331.

(53) Yokel, R. A.; Hussain, S.; Garantziotis, S.; Demokritou, P.; Castranova, V.; Cassee, F. R. The Yin: An Adverse Health Perspective of Nanoceria: Uptake, Distribution, Accumulation, and Mechanisms of Its Toxicity. *Environ. Sci.: Nano* **2014**, *1*, 406−428.

(54) Gagnon, J.; Fromm, K. M. Toxicity and Protective Effects of Cerium Oxide Nanoparticles (Nanoceria) Depending on Their Preparation Method, Particle Size, Cell Type, and Exposure Route. *Eur. J. Inorg. Chem.* **2015**, *2015*, 4510−4517.

(55) Immordino, M. L.; Brusa, P.; Rocco, F.; Arpicco, S.; Ceruti, M.; Cattel, L. Preparation, Characterization, Cytotoxicity and Pharmacokinetics of Liposomes Containing Lipophilic Gemcitabine Prodrugs. *J. Controlled Release* **2004**, *100*, 331−346.

(56) Malyukin, Y.; Maksimchuk, P.; Seminko, V.; Okrushko, E.; Spivak, N. Limitations of Self-Regenerative Antioxidant Ability of Nanoceria Imposed by Oxygen Diffusion. *J. Phys. Chem. C* **2018**, *122*, 16406−16411.